The Astrophysical Journal, 842:87 (14pp), 2017 June 20 https://doi.org/10.3847/1538-4357/aa74b8

Radio Luminosity Function of Flat-spectrum Radio Quasars

Peiyuan Mao[1], C. Megan Urry[1], Ezequiel Marchesini[2,3,4,5,6], Marco Landoni[2,3], Francesco Massaro[2,3], and Marco Ajello[7]
[1] Yale Center for Astronomy & Astrophysics, Physics Department, New Haven, CT 06520, USA
[2] Physics Department, University of Turin, via Pietro Giuria 1, I-10125 Turin, Italy
[3] Istituto Nazionale di Fisica Nucleare, Sezione di Torino, I-10125 Turin, Italy
[4] Facultad de Ciencias Astronomícas y Geofísicas, Universidad Nacional de La Plata, Paseo del Bosque, B1900FWA, La Plata, Argentina
[5] Instituto de Astrofísica de La Plata, CONISET-UNLP, CCT La Plata, Paseo del Bosque, B1900FWA, La Plata, Argentina
[6] Istituto di Astrofisica Spaziale e Fisica Cosmica di Bologna, via Gobetti 101, I-40129, Bologna, Italia
[7] Department of Physics and Astronomy, Clemson University, Kinard Lab of Physics, Clemson, SC 29634-0978, USA
Received 2017 January 16; revised 2017 April 24; accepted 2017 May 19; published 2017 June 16

Abstract

We present the radio luminosity function (LF) of flat-spectrum radio quasars (FSRQ), using the the largest and most complete sample to date. Cross-matching between the FIRST 20 cm and GB6 6 cm radio surveys, we find 638 flat-spectrum radio sources above 220 mJy at 1.4 GHz; of these, 327 are are classified and verified using optical spectroscopy data, mainly from Sloan Digital Sky Survey Data Release 12. We also considered flat-spectrum radio sources that lack both literature references and optical spectroscopy, and we identified 12 out of the 43 such sources to potentially be FSRQs, using their *WISE* colors. From the fully identified sample of 242 FSRQs, we derived the radio LF and cosmic evolution of blazars at 1.4 GHz, finding good agreement with previous work at 5 GHz. The number density of FSRQs increases dramatically to a redshift of $z \sim 2$ and then declines for higher redshifts. Furthermore, the redshift at which the quasar density peaks is clearly dependent on luminosity, with more luminous sources peaking at higher redshifts. The approximate best-fit LF for a luminosity-dependent evolutionary model is a broken power-law with slopes $\sim$0.7 and $\sim$1.7 below and above the break luminosity, $\log L_{1.4} \sim 43.8$ erg s^{-1}, respectively.

Key words: cosmology: observations – galaxies: active – galaxies: jets – quasars: general

Supporting material: extended figure, machine-readable tables

1. Introduction

Blazars are among the most energetic and common objects in the high energy sky, despite being a rare subclass of active galactic nuclei (AGNs). They are defined by flat radio spectra plus large amplitude, rapid variability of non-thermal emission across the electromagnetic spectrum (Urry & Padovani 1995). We understand blazars as AGN with Doppler-boosted relativistic jets pointing along the line of sight (Blandford & Rees 1978; Urry & Padovani 1995). The relativistic beaming of blazar jets results in interesting observational characteristics explaining most blazar features, and the numbers and properties of misdirected blazars are consistent with radio galaxies (Padovani & Urry 1990, 1991, 1992).

Blazars can be divided into two subclasses on the basis of their optical spectra: flat-spectrum radio quasars (FSRQ) having strong, broad emission lines, and BL Lac objects having weak or no emission lines (equivalent widths EW < 5 Å; Stickel et al. 1991).

Because relativistic jets cause the blazar phenomenon, all blazars emit strongly at radio wavelengths. Previous studies have identified radio emission as a fundamental property of blazars (Giommi & Padovani 1994; Giommi et al. 1995; Fossati et al. 1997). Recently, Mao et al. (2016) also found the entire SED of blazars could be constructed reasonably well, starting from the radio luminosity. The radio luminosity function (LF) of blazars directly probes the evolving energy distribution of their jets. Some theories link blazar evolution to the cosmic evolution of the spin states of massive black holes, where rotational energy is converted into the kinetic energy of the outflowing jet (Blandford & Znajek 1977). Therefore blazar LFs may provide crucial insights into black hole spin and the growth history of the host galaxy (Falomo et al. 2014).

While there have been numerous recent works on the X-ray LFs of blazars (Giommi & Padovani 1994; Rector et al. 2000; Wolter & Celotti 2001; Caccianiga et al. 2002; Beckmann et al. 2003; Padovani et al. 2007) and γ-ray (Salamon & Stecker 1994; Chiang & Mukherjee 1998; Hartman et al. 1999; Ajello et al. 2012), there have been relatively fewer determinations of radio LFs. Since blazars are rare among AGN (due to their small-angle orientation), previous samples used to construct radio blazar LFs were relatively small, and based on the brightest objects. Padovani & Urry (1992) constructed a 2.7 GHz radio LF for FSRQs from 50 sources from the 2 Jy sample using the classic $\sum 1/V_m$ method (Schmidt 1968). They found that FSRQs evolve positively, with $\langle V/V_m \rangle \approx 0.64$, and radio power evolving as $P(z) = P(0)\exp(T(z)/\tau)$, where $T(z)$ is the lookback time and $\tau = 0.23$ in units of the Hubble time. Wall et al. (2005) constructed a 2.7 GHz radio LF of quasars based on the Parkes 0.25 Jy sample, using the $\sum 1/V_m$ method binned in redshift and luminosity. They saw an increase in space density from low redshifts to $z \sim 1.5$, followed by a decline at higher redshift. Although their work was based on 355 objects, only 126 were spectroscopically confirmed quasars. Using the 1 Jy sample (Kuehr et al. 1981), Ricci et al. (2006) estimated the 5 GHz radio LF from 206 FSRQs, again using the $\sum 1/V_m$ method. In agreement with earlier works, they found positive evolution out to $z \sim 2.5$, followed by a decline. The most recent radio/microwave LF of FSRQs was calculated by Giommi et al. (2009) using 137 FSRQs from the WMAP3 sample at 41 GHz (much higher in frequency than the other radio surveys); they also saw positive evolution, with $\langle V/V_m \rangle \approx 0.62$.

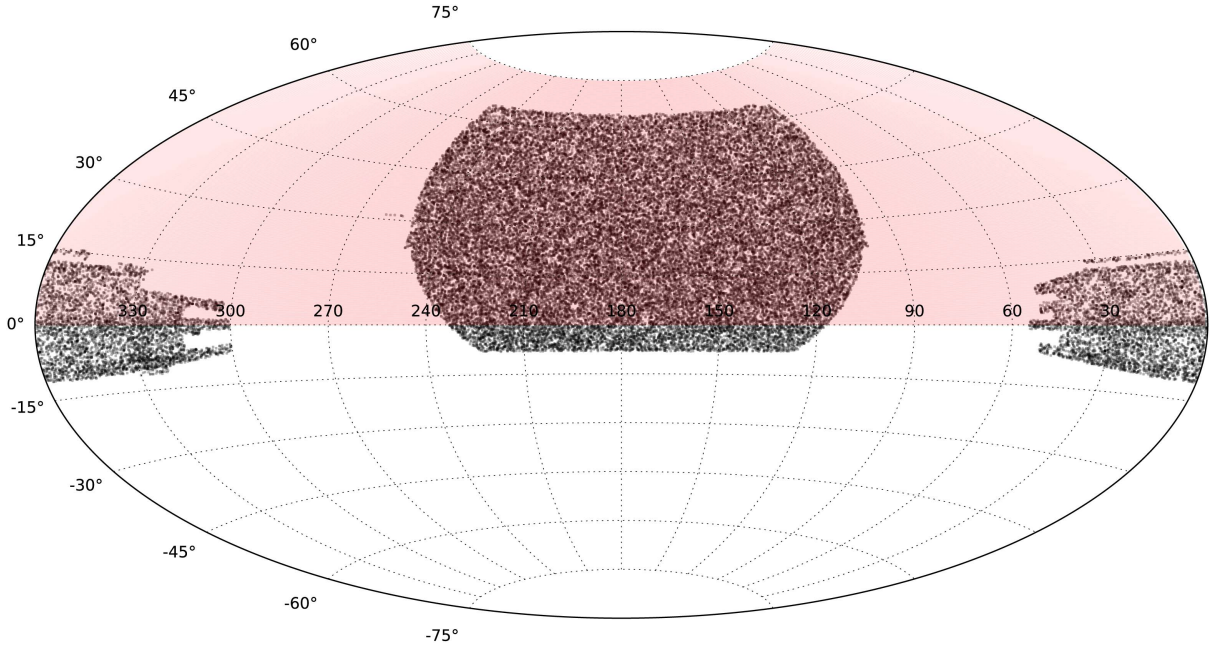

Figure 1. Areas covered by the FIRST (black points) and GB6 (red shaded region) radio surveys, in equatorial coordinates using a Hammer-Aitoff projection, showing the ∼9500 square degrees in common.

In this paper, we compute the 1.4 GHz LF measured from a sample of 285 FSRQs detected in the FIRST and GB6 radio surveys, 200 of which we personally verified as FSRQs based on published optical spectra.

This is roughly double the size of earlier spectroscopically validated FSRQ samples. In Section 2, we describe the sample selection, including the data used, the cross-matching between the two radio surveys, and the optical classifications, many of which were previously unpublished and/or not verified explicitly. Section 3 presents the derivation of the LF of FSRQs and discusses possible sources of uncertainty. In Section 4 we discuss the implications of our LF and state our conclusions.

We use cgs units unless otherwise stated. The spectral index, α, is defined as the power-law exponent of the flux density, $S_\nu \propto \nu^{-\alpha}$. The cosmological parameters $H_0 = 70\ \mathrm{km\ s^{-1}\ Mpc^{-1}}$ and $\Omega_\Lambda = 0.72$ (Hinshaw et al. 2013) are used, with the exception of the section where we compare our LF with previous works that used a different cosmology. All references of the logarithmic function are in base 10.

2. Sample Selection

2.1. Radio Cross-matches

To build the largest sample of flat-spectrum radio quasars, we started with the radio catalog of the Faint Images of the Radio Sky at Twenty Centimeter (FIRST) survey (White et al. 1997; Helfand et al. 2015), which covered 10,575 $\mathrm{deg^2}$ of the sky (8,444 $\mathrm{deg^2}$ in the north Galactic cap and 2131 $\mathrm{deg^2}$ in the south Galactic cap); and the Green Bank 6 cm (GB6) Radio Source Catalog (Gregory et al. 1996), which covered 17,000 $\mathrm{deg^2}$ of the sky at $0^\circ < \delta < 75^\circ$. The specific choice of the FIRST survey was because it covers much the same area as the Sloan Digital Sky Survey (SDSS; Ahn et al. 2012), which maximizes the chances of having optical photometry and spectrum for each of the sources to use in further classification and analyses. GB6 was chosen since it also has good overlap with FIRST (Figure 1). Figure 1 shows the largely overlapping footprints of the FIRST (the black region) and GB6 (the red region) surveys.

We cross-matched the radio position of each FIRST source with sources in the GB6 catalog, taking into account the positional uncertainties of both radio surveys. This led to an initial sample of 18,273 common objects among the 946,432 sources in the FIRST catalog and the 75,162 sources in the GB6 catalog.

To test for the probability of spurious matches, we used the following statistical approach. We built 100 mock replicas of the GB6 catalog by shifting each source position in a random direction of the sky by a fixed length of 5′. This shift, adopted to create a set of mock GB6 catalogs, was chosen to be not too far from the original position and within the FIRST footprint. This allowed us to obtain fake catalogs with a sky distribution similar to the original GB6, and to perform the cross-match, taking into account the local density distribution of radio sources. The total number of GB6 sources in each mock catalog was also preserved.

For each mock catalog, we counted the number of associations, with the FIRST occurring at angular separations R smaller than 300″. Then we computed the mean number $\lambda(R)$ of these mock associations, averaged over the 100 fake catalogs, and we verified that $\lambda(R)$ has a Poisson distribution. Increasing the radius by $\Delta R = 0\farcs5$, we also computed the difference $\Delta\lambda(R)$ as

$$\Delta\lambda(R) = \lambda(R + \Delta R) - \lambda(R). \quad (1)$$

We then compared $\Delta\lambda(R)$ with the number of real associations (i.e., $\Delta N(R)$) occurring within the same ΔR.

In Figure 2 we show the comparison between $\Delta N(R)$ and $\Delta\lambda(R)$. For radii larger than $R_{\max} = 160''$, the $\Delta\lambda(R)$ curve superimposes that of $\Delta N(R)$, indicating that GB6-FIRST cross-matches could occur and be spurious.

Then we computed the probability of spurious associations $p(R)$ as the ratio between $N(R)$ and $\lambda(R)$, corresponding to a

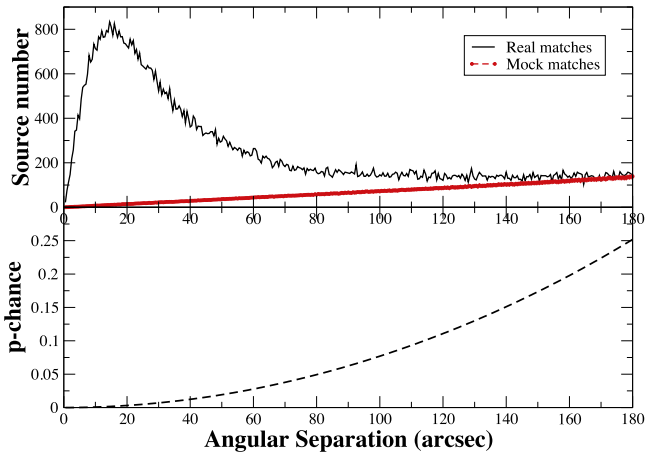

Figure 2. Simulations show that the rate of mismatches between FIRST and GB6 radio sources is not significant as long as the cataloged positions are within ∼1 arcmin (<5% chance of spurious association). Upper panel: The values of $\Delta\lambda(R)$ (red line) and $\Delta N(R)$ (black line) as a function of the angular separation R. Lower panel: The probability of having spurious associations $p(R)$ as a function of the angular separation R.

value of ∼5% at the peak of the $\Delta N(R)$ distribution (see, e.g., Massaro et al. 2013d, 2014b, 2014a, for a similar procedure to estimate the probability of spurious associations).

Using the integrated flux densities at 1.4 GHz from FIRST and at 4.85 GHz from GB6, we computed the radio spectral index, α_r, for each of the 18,273 cross-matched radio sources. We then identified those radio sources with flat spectra ($\alpha_r < 0.5$), which cut the sample to 11,452 sources.

Since the FIRST and GB6 surveys have different flux (completeness) limits—∼1 mJy (10 mJy) and ∼18 mJy (50 mJy), respectively—we have to cut the cross-matched flat-spectrum sample at a high enough flux limit that it is complete for flat-spectrum or even rising sources (i.e., at least a few times 50 mJy at 1.4 GHz). We chose a conservative limiting flux density of 220 mJy at 1.4 GHz, which gives 638 flat-spectrum radio sources. As a check, we note that these objects all have firm, unambiguous matches; specifically, out of 393 FIRST sources that have nearby companions (within one degree), every single companion is 100–1000 times fainter than the primary source (i.e., it is simply a random background source). This means we have selected a bright sample with unambiguous flat-spectrum counterparts in both catalogs. It is technically possible that we may still be missing true flat-spectrum sources due to the non-simultaneity of the FIRST and GB6 observations, but with such a conservatively high flux cut, the required variability would have to be much higher than the factors of 2–3 typically observed in radio quasars; moreover, these will be random omissions and thus will not change our result, except in terms of the normalization.

2.2. Optical Classification

The FIRST radio survey was carried out, by design, over the footprint of the SDSS (Alam et al. 2015), allowing us to obtain optical spectroscopic information for a large fraction of the sources in our sample. This is crucial to down-selecting to a bona-fide FSRQ sample, defined as flat-spectrum radio sources with quasar-like broad optical emission lines.

Of the 638 radio sources with flat radio spectra, 327 have an optical spectrum available in the literature, 266 from SDSS and the rest from various other sources identified through the NASA Extragalactic Database (NED[8]). We inspected these optical spectra and classified them according to the criteria described in Véron-Cetty & Véron (2000), as BL Lac object (BLL), quasar (QSO), normal galaxy (GAL), Seyfert galaxy (SEY), or normal star (STAR). Figure 3 shows examples of the first four types of spectra.

Objects for which the available optical spectrum has a signal-to-noise ratio lower than 3 were labeled as NOISE (12 cases of SDSS spectra), while those for which we could not identify emission and/or absorption lines were marked uncertain (UNC).

Since the goal of our analysis is to build the LF of FSRQs, we want only sources that clearly show broad emission lines in the optical spectra. It is worth noting that the spectrum of a quasar at low redshift (i.e., $z < 0.3$) could, if it had a low signal-to-noise ratio and/or was observed over a narrow band, be classified as a Seyfert galaxy (Véron-Cetty & Véron 2000). Accordingly, we classified them as quasars because of their high radio luminosity ($\nu L_{\nu,1.4\,\mathrm{GHz}} > 5 \times 10^{41}\,\mathrm{erg\,s^{-1}}$; Peterson 1997). Below this level, any objects classified as Seyfert galaxies or normal galaxies are too under-luminous to have a powerful radio jet (Véron-Cetty & Véron 2000).

Of the remaining 311 sources without published spectra, 119 have reported redshifts and/or classifications in the literature, even though we could not confirm their identifications ourselves. Finally, for 113 of the 638 flat-spectrum sources, we could find no optical spectroscopic information; the impact of omitting these objects on the sample completeness is discussed in Section 2.5.

2.3. Contamination

Since we combined radio-flux density at 1.4 GHz from the FIRST survey (with a ∼5″ beam) and the GB6 4.85 GHz survey (with a ∼3.′5 beam), there is a difference of at least a factor of 40 in spatial resolution. This could lead to inaccurate flux arising from extended radio morphology and/or nearby radio sources in the estimate of the radio spectral index, which in turn could result in a flatter spectral index than what we estimated by combining the flux densities of the two surveys. Since we only care about the FSRQs in our sample, we adopted the following strategy to check the presence of this contamination.

First we cut out from the FSRQ sample all those sources that in the FIRST radio images show a distinct nearby source or extended radio emission associated within 3.′5 from the location of the optical-radio cross-match in the FSRQ sample, and having flux density grater than 10% of the source core value. This leads to the exclusion of 32 out of 45 QSOs and 11 out of 20 QSOs with extended morphology and/or nearby radio objects. These 43 sources are relatively low-redshift sources with a maximum redshift of $z = 1.9$.

Then we also performed cross-matches between our final sample and the CRATES sample (Healey et al. 2007), which is also a well-studied catalog of flat-spectrum radio sources. Using an angular separation of 5″, we found 405 out of the 638 sources in our sample are also in CRATES, and only two QSOs in our sample did not have a CRATES counterpart. Figure 4 shows the comparison between radio spectral indices calculated

[8] The NASA/IPAC Extragalactic Database (NED) is operated by the Jet Propulsion Laboratory, California Institute of Technology, under contract with the National Aeronautics and Space Administration. See https://ned.ipac.caltech.edu/.

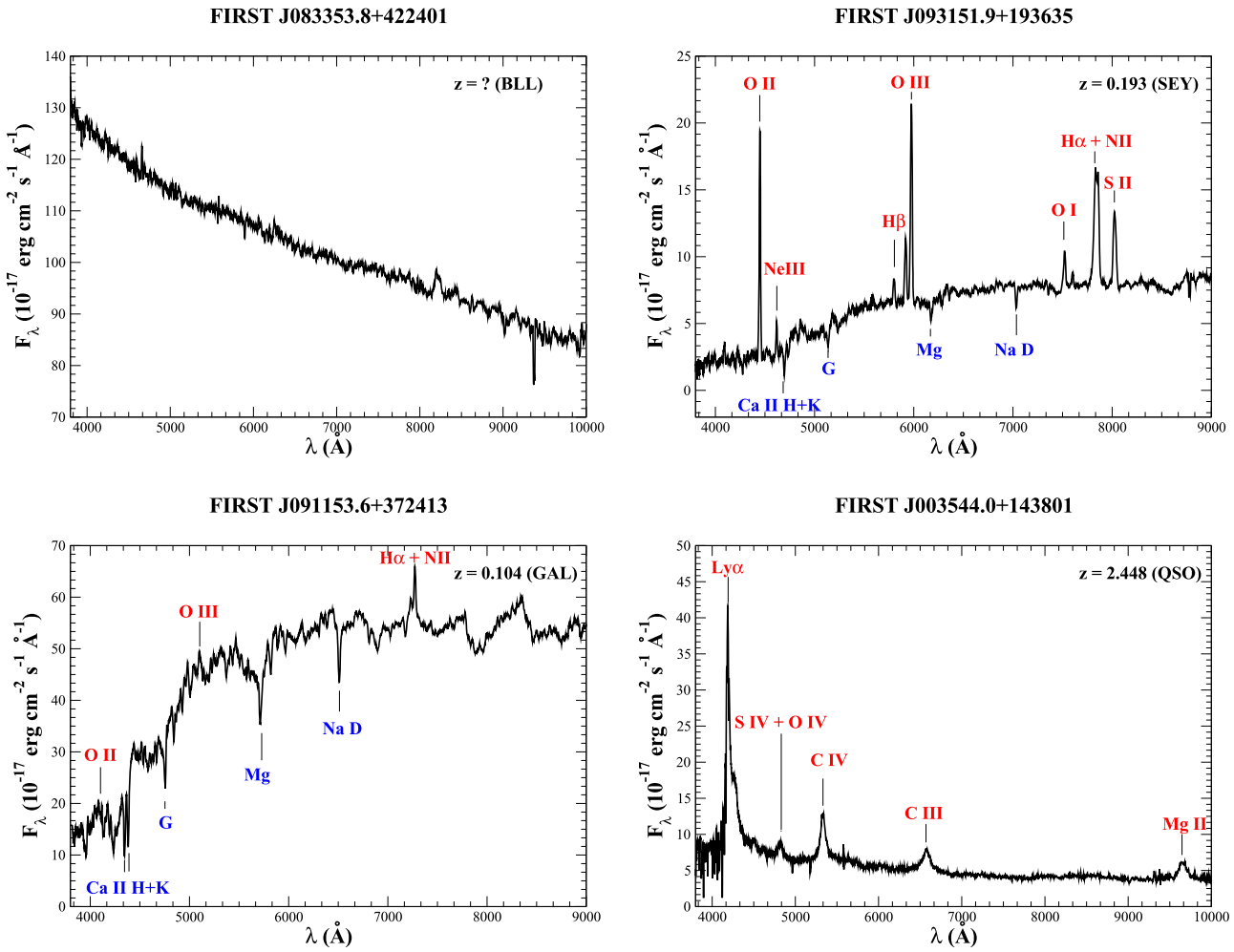

Figure 3. Examples of spectra corresponding to different classifications. Upper left panel: FIRST J083353.8+422401 has a featureless continuum and thus is classified as a BL Lac object at unknown redshift. Upper right panel: FIRST J093151.9+193635 is classified as a Seyfert galaxy at $z = 0.193$ because it has both high ionization emission lines and obvious galactic absorption features. Lower left panel: FIRST J091153.6+372413 is identified as a normal elliptical galaxy at redshift $z = 0.104$ because it lacks an AGN signature. Lower right panel: The $z = 2.448$ quasar FIRST J003544.0+143801 has very strong broad emission features and no visible contribution from a host galaxy. The main spectral emission and/or absorption features are marked in each figure. (An extended version of this figure is available.)

by us and by Healey et al. (2007) for the FSRQs in the clean and inclusive sample, and the estimates seem to be in agreement with only a small number of sources to be borderline cases. Seventeen QSOs in our sample indeed have a radio spectral index greater than 0.5, as calculated by Healey et al. (2007). On the other hand, two more steep ($\alpha > 0.5$) sources above our 220 mJy flux cut in the FIRST-GB6 cross-matched sample are certain quasars with a flat spectral index reported. We ran our fitting algorithm with a sample, excluding the 17 sources and including those 2 sources, and verified that the results were essentially unchanged.

The methodology for matching radio catalogs with differing spatial resolutions is discussed in detail by Kimball & Ivezić (2008), and we have also compared our cross-matches between FIRST and GB6 to those reported in that paper as a final sanity check. Apart from eight QSOs in our sample that are not included in Kimball & Ivezić (2008), all other cross-matches are identical between our sample and the Kimball et al. sample.

2.4. Final FSRQ Sample

Out of the 327 objects with optical spectra classified, 200 were classified as FSRQs (of which 168 are free from contamination), 26 were classified as BL Lacs, 38 were classified as Seyferts, 41 were classified as Galaxies, 2 were classified as stars, and 12 and 8 indicated as noisy or uncertain, respectively. An additional 85 quasars (of which 74 are free from contamination) out of the 119 with a literature description were also included in the inclusive sample. The composition of our sample is summarized in Table 1.

As a result, we have two final samples of FSRQs: a clean sample with 168 verified sources, and an inclusive sample with 242 sources. In Table 2 we report the FIRST and GB6 names for each source together with their coordinates, our classification, the redshift, and a flag to highlight those sources classified in the inclusive but not the clean sample (i.e., with classifications in the literature but not by us). Figure 5 shows the spectral index and the flux distributions of the clean and the inclusive sample.

2.5. LF Incompleteness

Throughout the sample selection process, several steps potentially introduced incompleteness into our FSRQ sample, and each is addressed here.

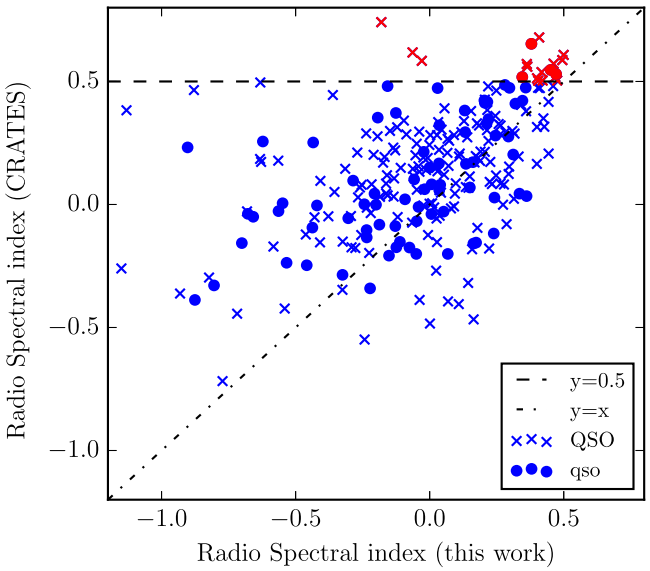

Figure 4. Comparison between the radio spectral indices for FSRQs in the clean and inclusive sample that are calculated by this work and by Healey et al. (2007). The calculations agree in general with very few border-line cases. There are seventeen objects in our sample with a steep radio spectrum ($\alpha > 0.5$), as reported in Healey et al. (2007), and we verified that the LF results are essentially unchanged with or without these 17 objects.

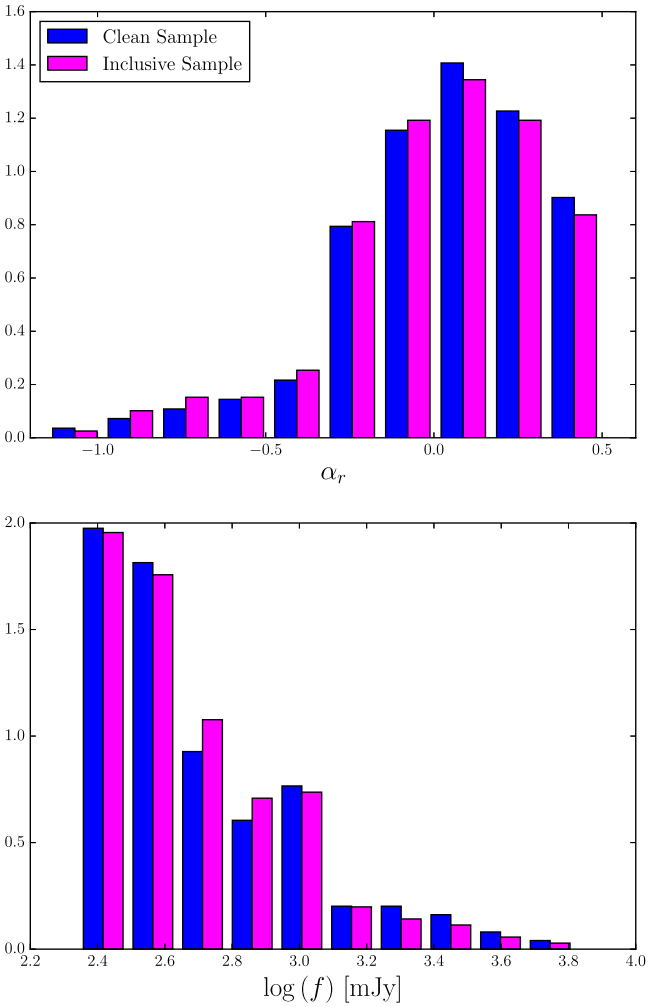

Figure 5. Spectral index (top) and flux (bottom) distributions of the inclusive FSRQ sample.

Table 1
Composition of 1.4 GHz Flux-limited Sample of Flat-spectrum Radio Sources

Class	# Clean[a]	# Inclusive[b]
Total	327	638
FSRQs[c]	168/200	242/285
BL Lacs	26	36
Seyferts	38	39
Galaxies	41	120
Star	2	23
Noise	12	12
Uncertain	8	10
Unknown	0	113

Notes.
[a] The number of sources with optical spectra available in the literature and classified consistently by us.
[b] The sample was extended by including sources that have published designations in the literature but no spectra.
[c] Smaller number represents the sample without possibly contaminated sources.

Since the spectral index α is inferred from the radio fluxes, the uncertainties of the flux measurements get propagated and resulted in an error $\Delta\alpha$,[9]

Using the same selection criteria we have used in building our sample, we find there are 697 sources above 200 mJy (chosen to be slightly lower than our sample flux limit) with a radio spectral index $\alpha \leqslant 0.5$, yet 187 of these have $\alpha + \Delta\alpha > 0.5$. In other words, these sources could have steep radio spectra and thus may need to be excluded from the sample. On the other hand, 256 sources with a flux density above 200 mJy have $\alpha > 0.5$ and $\alpha - \Delta\alpha \leqslant 0.5$; that is, these sources potentially have flat radio spectrum, in which case they ought to be included in our sample. With these two numbers, we estimate the incompleteness introduced by the cut on radio spectral index to be 10%.[10]

Out of the 638 sources in our sample, there are 113 sources of unknown classification, even after thorough searches in the literature (Section 2.2), and our LF would not be complete without investigating and addressing these sources. While we can not accurately classify them without spectroscopic data, there are ways to speculate about their true identities.

With the advent of the *WISE* observations, there are now selection techniques for AGN based on their mid-IR colors (e.g., Jarrett et al. 2011; Massaro et al. 2011; Stern et al. 2012; Assef et al. 2013; D'Abrusco et al. 2013, 2014; Mateos et al. 2013). Many of these methods were fine-tuned to identify AGN selected by mid-IR colors (i.e., *Spitzer*) or X-ray emission (e.g., Stern et al. 2005). It is worth mentioning that even at low frequencies (i.e., below ~1 GHz), radio observations combined with *WISE* data have been extremely useful for identifying new FSRQs (Massaro et al. 2013a, 2014a; Nori et al. 2014; Giroletti et al. 2016).

We then searched for *WISE* counterparts of our 638 sources, within 3.″3 of the FIRST position (D'Abrusco et al. 2013; Massaro et al. 2013a), obtaining 431 matches, with no object having more than one counterpart. Plotting the 388 sources with definite classifications on the *WISE* color space confirmed that the FSRQs in our inclusive sample show the mid-IR colors

[9] $\Delta\alpha = \frac{1}{\log(4.85\,/\,1.4)}\sqrt{\left(\frac{\Delta f_{1.4\,\mathrm{GHz}}}{f_{1.4\,\mathrm{GHz}}}\right)^2 + \left(\frac{\Delta f_{4.85\,\mathrm{GHz}}}{f_{4.85\,\mathrm{GHz}}}\right)^2}$.

[10] $(256 - 187)/697 = 0.099 \approx 10\%$.

Table 2
The Complete Data for the Radio-flux-limited Sample of Flat-spectrum Sources[a]

FIRST Name	GB6 Name	R.A.	Decl.	z	Class[b]	Clean[c]	α	$F_{\rm int}$[d]
FIRSTJ002903.5+050934	GB6 J0029+0509	7.2650	5.1597	1.6330	qso	No	0.1324	436.020
FIRSTJ002945.8+055440	GB6 J0029+0554B	7.4412	5.9113	1.3170	qso	No	−0.0754	303.760
FIRSTJ003544.0+143801	GB6 J0035+1438	8.9337	14.6338	2.4479	QSO	Yes	−0.2368	252.880
FIRSTJ012156.8+042224	GB6 J0121+0422	20.4869	4.3735	0.6370	qso	No	−0.2223	967.430
FIRSTJ014922.3+055553	GB6 J0149+0555	27.3432	5.9315	2.3450	QSO	Yes	−0.3243	1031.530
FIRSTJ020346.6+113445	GB6 J0203+1134	30.9445	11.5793	3.6390	qso	No	0.1499	971.510
FIRSTJ020706.9+065901	GB6 J0207+0659	31.7789	6.9837	0.3600	qso	No	−0.1253	641.380
FIRSTJ021748.9+014449	GB6 J0217+0144	34.4539	1.7471	1.7150	qso	No	−0.5337	789.510
FIRSTJ023407.1+044643	GB6 J0234+0446	38.5298	4.7786	2.0600	qso	No	0.0296	382.210
FIRSTJ023951.2+041621	GB6 J0239+0416	39.9636	4.2727	0.9780	qso	No	−0.2437	811.790
FIRSTJ024918.0+061951	GB6 J0249+0619	42.3250	6.3311	1.8810	qso	No	−0.0483	587.970

Notes.
[a] The full sample table contains 242 rows, and is available in a machine readable format online.
[b] Source classification: BL Lac object (BLL), quasar (QSO), normal galaxy (GAL), Seyfert galaxy (SEY), star (STAR), low signal to noise (NOISE), and uncertain (UNC). Capital letters indicate classification done via inspecting the optical spectrum, while small letters indicate classification obtained through literature.
[c] Clean if the source spectrum was optically verified.
[d] Integrated flux at 1.4 GHz, in units of mJy.

(This table is available in its entirety in machine-readable form.)

expected of this blazar subclass (D'Abrusco et al. 2012), and blazars are well separated from the generic extragalactic sources (D'Abrusco et al. 2014).

Another 43 matched sources are not classified by optical spectrum; these are a large fraction of the 113 flat-spectrum radio sources with unknown classification. To investigate the nature of these 43 objects, we compared their mid-IR colors with those of known blazars (Massaro et al. 2013b, 2013c) in the sample recently built to investigate the IR-gamma-ray connection (Massaro & D'Abrusco 2016). This sample contains 23,978 generic extragalactic sources (non-blazars), 426 FSRQs, and 610 BL Lacs. The 1036 blazars are selected from the most recent release of Roma-BZCAT (Massaro et al. 2015), and the generic IR sources are selected from *WISE* at high Galactic latitudes.

We utilized several machine learning algorithms and trained a classifier for the source class based on their *WISE* colors (W1−W2) and (W2−W3). To avoid the "class imbalance" problem,[11] we randomly split the generic class into 38 subclasses of 631 sources and trained 38 classifiers separately. The final classifier was taken as the average of the 38 trained sub-classifiers.

Several typical classification models were used, such as random forest (Breiman 2001), support vector machine (Cortes & Vapnik 1995), gradient boost (Friedman 2001), and so on, and we found out that the simple logistic regression algorithm gives the best result in the training sample, resulting in a prediction accuracy of 86.6 ± 0.3%. Using this classifier, 12 of the 43 unknown sources with *WISE* counterparts were predicted to be quasar-like objects. Figure 6 shows the classification result of these 43 sources on the *WISE* colors plot on top of the training sample. We conclude that 32 of the 113 unknown sources might be FSRQs missing from our sample:[12]

None of these 12 predicted quasar-like sources have a redshift reported in literature; instead, we estimated their redshifts using a K-Nearest Neighbor (KNN) regression calculated as a distance-weighted average (distance in the *WISE* colors plot) of the the redshifts of the FSRQs around them on the plot. Table 3 shows the name, redshift, and radio fluxes of these 12 sources. In Section 4 we calculated the best-fit LF, including these 12 quasar-like objects from the unknown sample, as well as for the clean and inclusive samples. These results are reported in Tables 4 and 5.

Combining these estimates, the total number of FSRQs in our sample could be as many as 301.[13] This means that the incompleteness correction for our clean, inclusive and unknown samples are 0.559, 0.805, and 0.845, respectively. This incompleteness is incorporated into our sky coverage function, and the $\log N$–$\log S$ plot of different samples would therefore end up perfectly overlapping, once we take it into consideration.

3. Luminosity Function

3.1. Method

We used the maximum-likelihood (ML) algorithm to compute the LF without loss of information by binning, as happens in the classic $\sum 1/V_m$ approach (Schmidt 1968). The ML method was first used for LFs by Marshall et al. (1983) and more recently has been used for sub-millimeter galaxies (Wall 2008) and blazars detected by *Swift* and *Fermi* (Ajello et al. 2009, 2012).

In the ML formulation, the spatial density of FSRQs as a function of their radio luminosity at 1.4 GHz and redshift

[11] In our case, the number of generic sources (23,978) ≫ the number of blazars (1036). Any classifier that naïvely predicts everything to be generic would have a high accuracy of more than 95%, making the accuracy a terrible measure of classifier strength, and any classifier trained under this setting would be highly inaccurate.

[12] $12/43 \times 113 = 31.5$.

[13] $(242 + 12/43 \times 113) \times (1 + 0.099) = 300.6$.

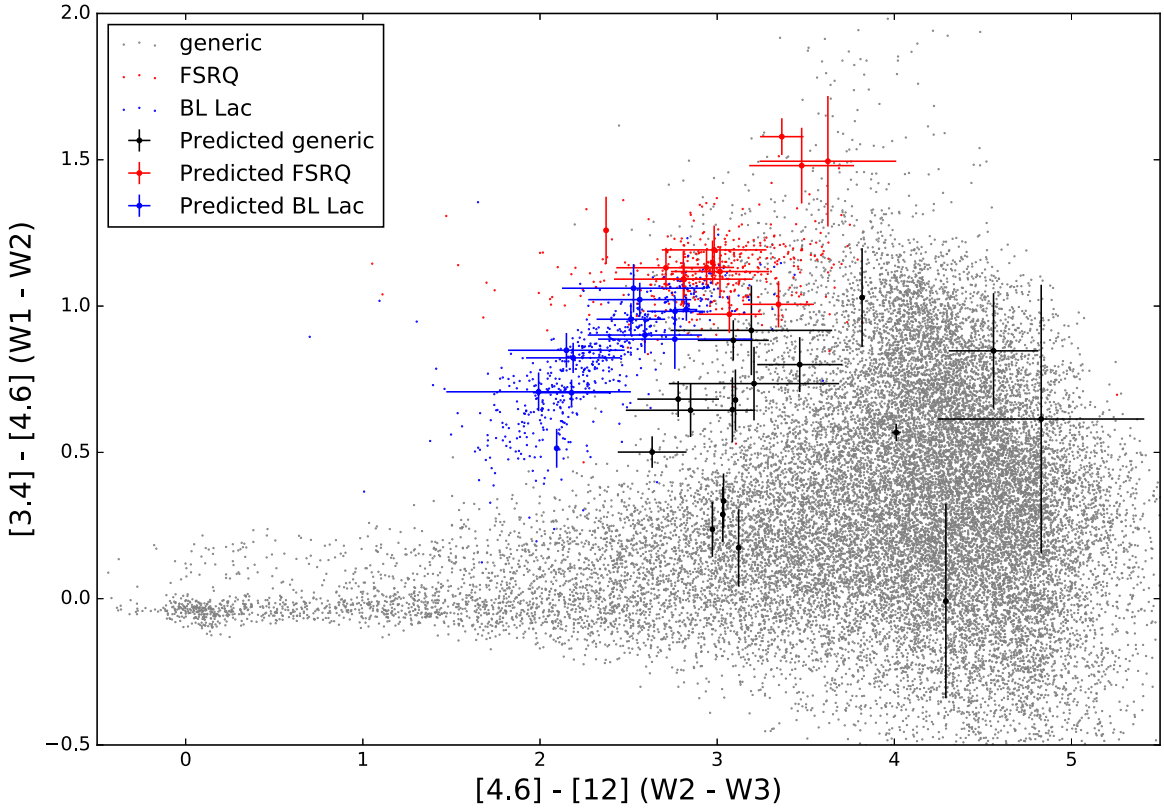

Figure 6. *WISE* colors of a training set (black points) and the 43 of the 113 unknown sources that have *WISE* mid-IR counterparts within 3.″3. Red crosses are identified as FSRQs, blue crosses as BL Lacs, and black crosses as other, using a logistic regression model trained from a sample built by Massaro & D'Abrusco (2016) to investigate the IR-gamma-ray connection. The training sample consists of 426 FSRQs, 610 BL Lacs, and 23978 generic sources, and our classifier was able to achieve an average prediction accuracy of 86.6 ± 0.3% after addressing the "class imbalance" problem.

Table 3
13 Sources with Unknown Classification Predicted To Be FSRQs

Name	z^{a}	$f_{1.4\,\mathrm{GHz}}$ [mJy]
FIRST J072820.5+215306	1.29	595.34
FIRST J120827.5+541319	1.57	461.30
FIRST J092314.4+384939	1.58	403.55
FIRST J233257.6+083810	1.51	357.56
FIRST J074956.9+575014	0.80	351.36
FIRST J150407.5+324921	1.78	338.15
FIRST J071055.3+492404	1.48	289.53
FIRST J142717.2+114253	1.71	240.80
FIRST J230844.1+094626	1.25	237.78
FIRST J131214.2+253113	0.79	237.19
FIRST J101051.8+333017	1.47	225.98
FIRST J214655.1+042725	1.43	221.48

Note.
[a] The redshifts are estimated from the redshifts of similar FSRQs using the KNN algorithm.

(This table is available in machine-readable form.)

$(d^2N/dLdz)$ is given by the function

$$\frac{d^2N}{dL\,dz} = \frac{d^2N}{dLdV} \times \frac{dV}{dz} = \Phi(L, z) \times \frac{dV}{dz}, \qquad (2)$$

where $\Phi(L, z)$ is the LF and dV/dz is the co-moving volume element per unit redshift and per solid angle.

The best-fit LF is then found by comparing the number of expected objects to the observed number (considering detection limits and selection effects, details below) through an ML estimator. In Equation (2), luminosity-redshift space is divided into fine intervals of size $dL\ dz$. Defining the number density of FSRQs at luminosity L and redshift z as $\lambda(L, z)$, the expected number of FSRQs in that small interval is

$$\lambda(L, z)\,dL\,dz = \Phi(L, z)\Omega(L, z) \times \frac{dV}{dz}\,dL\,dz, \qquad (3)$$

where $\Omega(L, z)$ is sky coverage, evaluated as the product of the survey solid angle, the incompleteness correction (see Section 2.5), and the probability of detecting in the survey an FSRQ with luminosity L and redshift z. The overlap of the FIRST and GB6 survey footprints is roughly 9500 deg^2, which is about 23% of the sky, or a total solid angle of $0.23 \cdot 4\pi = 2.89$ sr. The detection probability for the FIRST survey is a simple step function with value 1 for observed flux greater than 220 mJy and 0 otherwise.

Taking the limit as $dL \to 0$ and $dz \to 0$ in the usual way, λ becomes either 0 or 1 for either no FSRQ detected or exactly one FSRQ detected. The likelihood function based on joint Poisson probabilities is then

$$L = \prod_i \lambda_i\,dLdz\,e^{-\lambda_i\,dL\,dz} \times \prod_{j,j\neq i} e^{-\lambda_j dL\,dz}, \qquad (4)$$

Table 4
Best-fit Parameters of the Pure Luminosity Evolution LF[a]

Sample	# Objects	A[b]	γ	k	ξ
Clean	168	1.63E+02	1.32 ± 0.09	6.37 ± 0.56	−0.50 ± 0.05
Inclusive	242	1.47E+02	1.37 ± 0.08	6.52 ± 0.47	−0.50 ± 0.04
Ext + Unknown	254	1.40E+02	1.37 ± 0.08	6.52 ± 0.47	−0.48 ± 0.04

Notes.
[a] Parameters without an error estimate were kept fixed during the fit.
[b] In units of 10^{-13} Mpc^{-3} erg^{-1} s.

Table 5
Best-fit parameters of the Luminosity-dependent Density Evolution LF

Sample	# Objects	A[a]	γ_1	L_*[b]	γ_2	z_c^*	α	p_1	p_2
Clean	168	7.35E+04	0.67 ± 0.20	6.00 ± 3.03E+00	1.69 ± 0.16	1.94 ± 0.22	0.08 ± 0.05	4.54 ± 0.85	−7.81 ± 3.24
Inclusive	242	9.87E+05	0.46 ± 0.31	6.91 ± 6.89E-01	1.52 ± 0.14	1.93 ± 0.22	0.04 ± 0.05	5.16 ± 0.80	−5.26 ± 2.17
Ext + Unknown	254	9.40E+05	0.46 ± 0.32	6.91 ± 6.60E-01	1.52 ± 0.14	1.93 ± 0.23	0.05 ± 0.05	5.16 ± 0.85	−5.26 ± 2.18

Notes.
[a] In units of 10^{-13} Mpc^{-3} erg^{-1} s.
[b] In units of 10^{43} erg s^{-1}.

where the first product is the joint probability density of observing each blazar in our sample in the infinitesimal bin of (L_i, z_i) having exactly one FSRQ, and the second product is the joint probability of observing zero FSRQs in all other bins (L_j, z_j), where $j \neq i$. Considering the log likelihood ($B = -2 \ln L$) and dropping constant terms, we get

$$B = -2 \sum_i \ln \frac{d^2N}{dL\, dz} + 2 \int_{z_{\min}}^{z_{\max}} \int_{L_{\min}}^{L_{\max}} \lambda\, dL\, dz. \quad (5)$$

The limits of integration used in Equation (5) were $z_{\min} = 10^{-2}$, $z_{\max} = 6$, $L_{\min} = 10^{38}$ erg s^{-1}, and $L_{\max} = 10^{46}$ erg s^{-1}. While the results of the analysis do not depend on the upper limits of integration, $z_{\max}$ or $L_{\max}$ (as long as they are higher than observed values for the sample), the lower limits $z_{\min}$ and $L_{\min}$ were chosen to be a few times lower than the minimum values observed in our data so that the low-luminosity, low-redshift FSRQs are accounted for.

To visualize the fitted LF, we compare observed quantities to those predicted by the LF (Figures 7, 8). Specifically, we plot the following three distributions:

$$\frac{dN}{dz} = \int_{L_{\min}}^{L_{\max}} \lambda(L, z) dL, \quad (6)$$

$$\frac{dN}{dL} = \int_{z_{\min}}^{z_{\max}} \lambda(L, z) dz, \quad (7)$$

and

$$N(>S) = \int_{z_{\min}}^{z_{\max}} \int_{L(z,S)}^{L_{\max}} \Phi(L, z) dL\, dz, \quad (8)$$

using the same integration limits as before, where $L(z, S)$ represents the minimum luminosity of an FSRQ at redshift z with a flux limit of S.

We also display the observed LF (Φ°, Figure 9), where (Ajello et al. 2009, 2012)

$$\Phi^\circ(L_i, z_j) = \Phi^p(L_i, z_j) \frac{N_{ij}^o}{N_{ij}^p}. \quad (9)$$

Here, L_i is the median value of the ith luminosity bin, and z_i is the jth redshift bin within that luminosity bin; the predicted number density, $\Phi^p(L_i, z_j)$, is the best-fit LF evaluated at these median luminosity and redshift values; and N_{ij}^o and N_{ij}^p are the observed and predicted number of FSRQs in the bin.

3.2. Pure Luminosity Evolution

The space density of radio-quiet AGN is known to be maximal at intermediate redshift. The epoch of this redshift peak correlates with source luminosity (Ueda et al. 2003; Hasinger et al. 2005), perhaps due to the combined effect of supermassive black hole growth over cosmic time and a falloff in fueling activity as the rate of major mergers decreases at late times. To test whether this is also true of the FSRQ population, we fit the data using a pure luminosity evolution (PLE) model of the form

$$\Phi(L, z) = \Phi(L/e(z)), \quad (10)$$

where

$$\Phi(L/e(z=0)) = \frac{A}{(\ln 10) L} \left[\left(\frac{L}{L_*} \right)^{\gamma_1} + \left(\frac{L}{L_*} \right)^{\gamma_2} \right]^{-1}, \quad (11)$$

and

$$e(z) = (1 + z)^k e^{z/\xi}. \quad (12)$$

In this formulation, only the luminosity evolves, and positive evolution ($k > 0$) indicates that the FSRQs were more luminous in the past and vice versa. From Equation (12), it is also apparent that the luminosity evolution of FSRQs peaks at $z_c = -1 - k\xi$. While the PLE LF is generally represented as a double power-law, as in Equation (11), our algorithm failed to converge, indicating that this functional

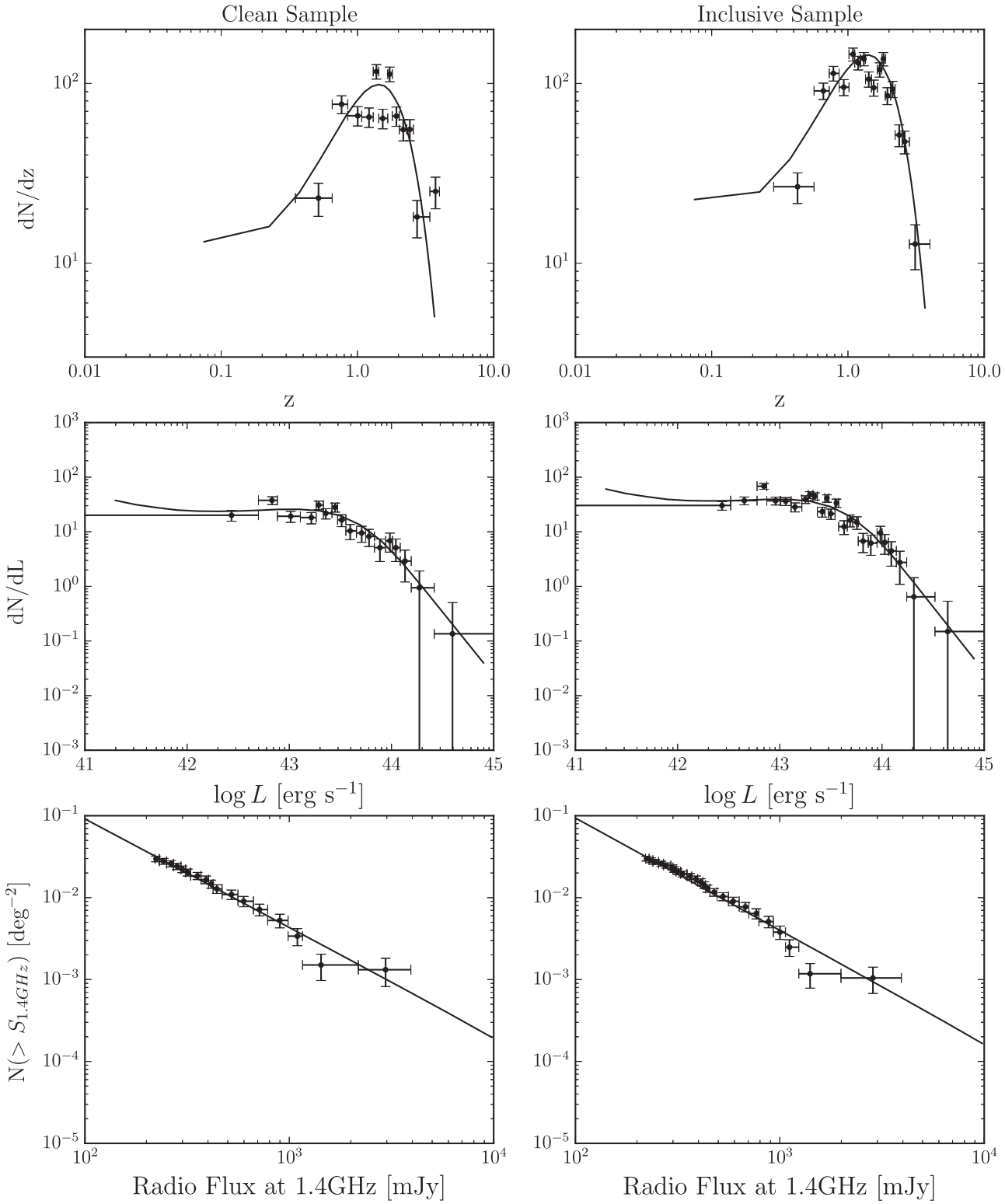

Figure 7. Redshift (top), luminosity (middle), and source count (bottom) distributions for FSRQs under the assumption of pure luminosity evolution. The lines show the best-fit PLE model using the clean sample (left) and the inclusive (right) sample. The data (points) agree reasonably well with the model. Fitted parameters are reported in Table 4.

form indeed describes our sample poorly. Specifically, L_* had too much freedom, and γ_1 and γ_2 also became highly correlated. Our sample demanded an LF in the form of a single power-law with one slope.

We therefore modified Equation (11) to

$$\Phi(L/e(z=0)) = \frac{A}{(\ln 10)} L^{-\gamma-1}. \quad (13)$$

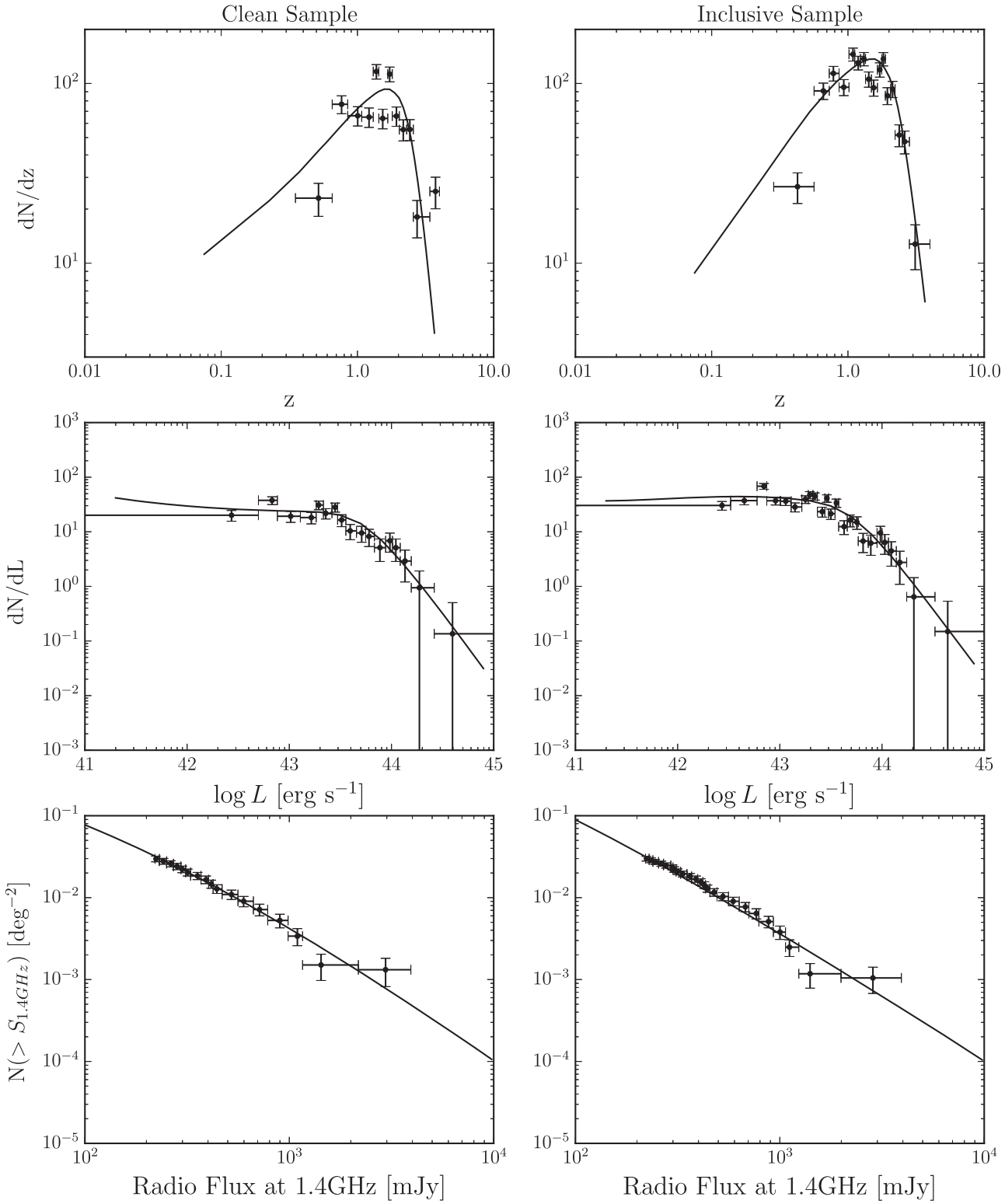

Figure 8. Redshift (top), luminosity (middle), and source count (bottom) distributions of FSRQs under the assumption of luminosity-dependent density evolution. The lines show the best-fit LDDE model using the clean sample (left) and the inclusive (right) sample. According to the log likelihood, these fits are better than the PLE fits, especially for the inclusive sample. Fitted parameters reported in Table 5.

Best-fit values for the fit parameters (A, γ, k, ξ) are reported in Table 4 for both the clean and inclusive samples, and the distributions in Equations (6), (7), and (8) are shown in Figure 7. It is clear that the FSRQs exhibit positive evolution, with best-fit $k = 6.37 \pm 0.56$ (for the clean sample) and redshift peak at $z_c = 2.19$. The subsequent rate of decrease of the luminosity above the peak redshift is well constrained ($\xi = -0.50 \pm 0.05$).

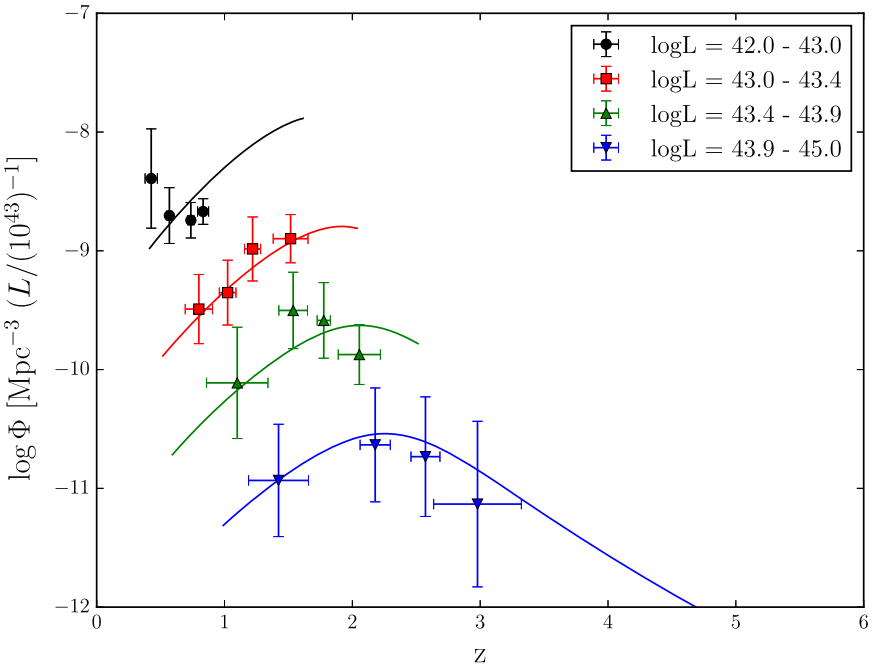

Figure 9. Evolution of FSRQ in four luminosity bins, using the best-fit LF with the LDDE description of evolution, shows that the space density of the most luminous FSRQs peaks earlier in the history of the universe, while the bulk of the population (i.e., the low-luminosity objects) peaks at later times. The y-axis is the log of the space density of FSRQ (i.e., number per unit volume, per unit luminosity normalized to 10^{43} erg s^{-1}, making the ordinate 10^{43} times the number per Mpc^3). The lines are the best-fit LF evaluated at the median luminosities of each bin, $\log L = 42.80$ (black), 43.27 (red), 43.64 (green), 44.12 (blue) erg s^{-1}; the data points are evaluated using Equation (9). The redshift range for each bin is limited by requiring at least one source within the volume and sensitivity limits of the radio survey.

3.3. Luminosity-dependent Density Evolution and the Redshift Peak

AGN populations tend to have luminosity-dependent density evolution (LDDE; Ueda et al. 2003; Ajello et al. 2012), so we also fit the FSRQ to a model of this type, in which the evolution is primarily in density with a luminosity-dependent redshift peak,

$$\Phi(L, z) = \Phi(L) \times e(z, L), \tag{14}$$

where

$$e(z, L) = \left[\left(\frac{1+z}{1+z_c(L)}\right)^{-p1} + \left(\frac{1+z}{1+z_c(L)}\right)^{-p2}\right]^{-1}, \tag{15}$$

and

$$z_c(L) = z_c^* \cdot (L/L_{\rm factor})^{\alpha}. \tag{16}$$

$\Phi(L, z)$ is the same double power-law as in Equation (11). This parameterization is similar to that used by Ueda et al. (2003), but is continuous around the redshift peak $z_c(L)$, which has the advantage for the fitting algorithm of smooth derivatives of the fitting function. Therefore the $z_c(L)$ term corresponds to the (luminosity-dependent) redshift where the evolution changes sign, with z_c^* being the redshift peak for an FSRQ with a luminosity of $L_{\rm factor}$ (trial and error leads to $L_{\rm factor} = 10^{43}$ erg s^{-1}).

The LDDE model provides a good fit to the FSRQ sample, reproducing the observed distributions in Figure 8. The fitted parameters are reported in Table 5, and the ratio of the log-likelihoods indicates a better fit for the LDDE than the PLE model (marginal improvement for the clean sample, significant improvement for the inclusive sample).

The parameters also confirm that the redshift of maximum space density increases with increasing luminosity. (The power-law index of the redshift-peak evolution is $\alpha = 0.08 \pm 0.05$.) This redshift evolution can be seen in Figure 9, which shows the change in space density for different luminosity bins.

3.4. Comparison with Previous Results

To obtain the model LF of FSRQ at redshift $z = 0$, we de-evolve the luminosities (PLE) or densities (LDDE) according to the best-fit parameters. To compare to survey data, we extrapolate the luminosities and densities according to the appropriate evolution (with either PLE or LDDE best-fit parameters) and then use the $\sum 1/V_{\rm max}$ method (Schmidt 1968) to construct the observed LF at $z = 0$. Ordinarily, the maximum volume for a source corresponds to the maximum redshift at which it would still be above the flux limit of the sample. Here we weigh the maximum volume $V_{\rm max}$ by the PLE or LDDE evolution:

$$V_{\rm max} = \int_{z_{\rm min}}^{z_{\rm max}} \Omega(L_i, z) \frac{e(z, L_i)}{e(z_{\rm min}, Li)} \frac{dV}{dz}\, dz, \tag{17}$$

where L_i is the source luminosity, $z_{\rm max}$ is the redshift above which the source drops out of the survey, and $e(z, L_i)$ is the evolution term defined in Equation (15), normalized at the minimum redshift $z_{\rm min} = 0$ to which the LF is to be de-evolved.

In the LF, the individual uncertainties of each of the best-fit parameters are reported in Tables 4 and 5. These were found by minimizing Equation (5) and then varying the parameter of interest while the others float. The process is repeated until a variation of $\Delta B = 1$ is achieved, which provides an estimate of the 68% confidence interval for that parameter (Avni 1976).

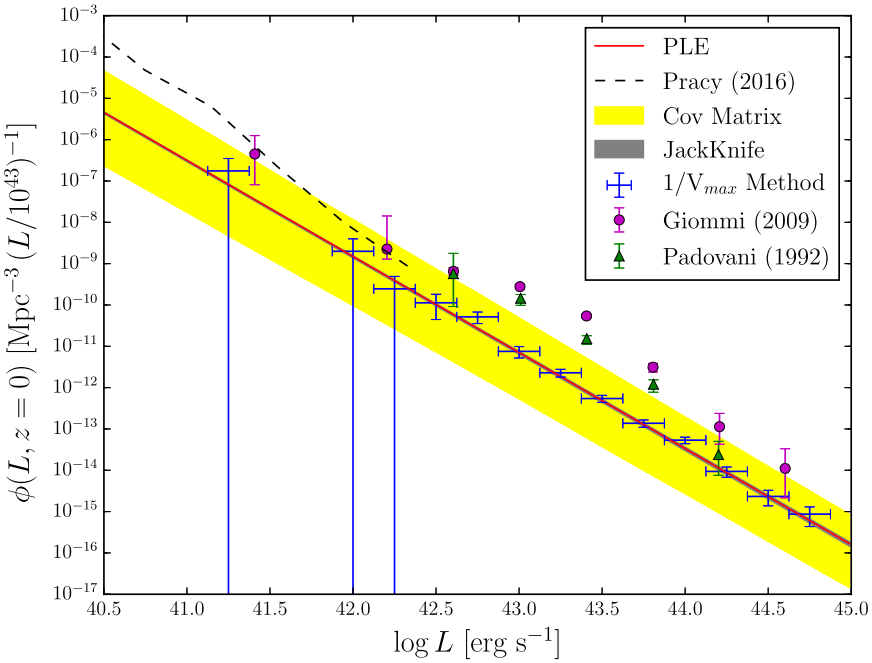

Figure 10. Local (de-evolved) FSRQ radio luminosity function derived from the best-fit PLE model in Section 3.4 (red solid line). The gray band represents the $\pm 1\sigma$ uncertainty computed using the Jack-knife method, and the yellow band indicates the $\pm 1\sigma$ uncertainty computed using the covariance matrix from the fitting algorithm (see Section 3.4 for details). The circles and triangles show the radio LFs derived by Giommi et al. (2009) and Padovani & Urry (1992), respectively, and the blue crosses show the LF computed from our inclusive sample using the classical $1/V_{\rm max}$ method developed by Schmidt (1968). The radio LF for high-excitation radio galaxies (HERG) constructed by Pracy et al. (2016) is also shown in comparison (black dashed line), as FSRQs are expected to be a subset of the HERG population.

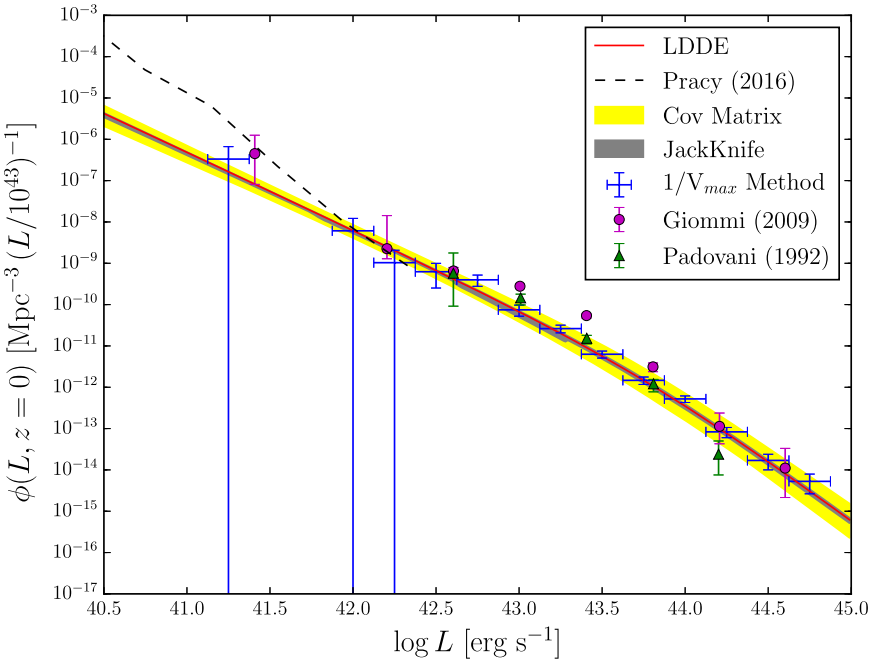

Figure 11. Local (de-evolved) FSRQ radio luminosity function derived from the best-fit LDDE model in Section 3.4 (red solid line). The gray band represents the $\pm 1\sigma$ uncertainty computed using the Jack-knife method, and the yellow band indicates the $\pm 1\sigma$ uncertainty computed using the covariance matrix from the fitting algorithm (see Section 3.4 for details). The circles and triangles show the radio LF derived by Giommi et al. (2009) and Padovani & Urry (1992), respectively, and the blue crosses show the LF computed using the classical $1/V_{\rm max}$ method developed by Schmidt (1968). The LDDE model clearly fits much better than the PLE model in Figure 10. The radio LF for high-excitation radio galaxies (HERG) constructed by Pracy et al. (2016) is also shown in comparison (black dashed line), as FSRQs are expected to be a subset of the HERG population.

Since $\Phi(L, z)$ has multiple parameters in both the PLE and the LDDE models, its uncertainties were calculated by applying a Jack-knife method, as well as making use of the covariance matrix from the fitted result. In the Jack-knife process, one of the 200 sources is omitted and the LF re-fitted; then the process is repeated, leaving out a different source each time. The gray bands in Figures 10 and 11 show the range of the resulting 200 fitted LFs, and we take this band to

be the statistical uncertainty on the space density. As an alternative approach, we did a Monte-Carlo simulation, drawing 1000 sets of parameters from the covariance matrix, taking into account the correlations among the parameters of the model. The re-sampled parameters were then used to compute the $\pm 1\sigma$ error of the LF at $z = 0$. In Figures 10 and 11, the yellow bands indicate the LF errors computed using the covariance matrix. The local LF agrees well with the one obtained through the $\sum 1/V_{\rm max}$ approach, and the LDDE model agrees better than the PLE model. The gray and yellow bands also show the true statistical uncertainty on the space density that is not captured by the $\sum 1/V_{\rm max}$ method.

The PLE local LF can be parameterized as a power-law

$$\Phi(L) = \frac{dN}{dL} = A \cdot L^{-\gamma}, \tag{18}$$

where $A = 7.07 \times 10^{-12}$ and $g = 1.32 \pm 0.04$. The LDDE local LF can be parameterized as a broken power-law with

$$\Phi(L) = \frac{dN}{dL} = A\left[\left(\frac{L}{L_*}\right)^{\gamma_1} + \left(\frac{L}{L_*}\right)^{\gamma_2}\right]^{-1}, \tag{19}$$

where $A = 1.83 \times 10^{-11}$, $L_* = 5.23 \pm 6.12$, $\gamma_1 = 0.89 \pm 0.10$, and $\gamma_2 = 1.93 \pm 0.35$. Both L and L_* are normalized to $L_{\rm factor}$, which is 10^{43} erg s^{-1}.

Other models do not generally provide as good a fit. The value of power-law indices found here (γ for PLE and γ_1, γ_2 for LDDE) are in good agreement with previous studies (Padovani & Urry 1992; Padovani et al. 2007; Giommi et al. 2009; Pracy et al. 2016).

4. Conclusion

We have calculated a new LF for flat-spectrum radio quasars using samples derived from cross-matching the FIRST and the GB6 radio surveys. The optical spectra of every single source in the clean sample containing 200 FSRQs above 220 mJy (of which 168 are free from contamination) were checked and verified. This sample is two to four times larger than previous clean FSRQ samples used for LFs (Padovani & Urry 1992; Wall et al. 2005; Ricci et al. 2006; Giommi et al. 2009). Another 311 flat-spectrum sources have no published optical spectrum, but 85 of these are classified as FSRQs in the literature, so we also defined an inclusive sample containing 285 FSRQs (of which 242 are free from contamination). This is by far the largest and most complete radio sample used for determining the LF of FSRQs.

The parameters of the LF were computed using a maximum-likelihood estimator on the unbinned data. This is more accurate than previous FSRQ LFs derived using the $\sum 1/V_m$ method, because that method requires binning. The best-fit parameters for the LFs based on the clean sample and on the inclusive sample for the LFs obtained from these two samples are consistent within the uncertainties.

The LF provides insight into the cosmological evolution of blazars. We found the space density of FSRQs increases rapidly with redshift until $z \sim 2$ and then decreases to higher redshift, consistent with previous results (Schmidt et al. 1995; Boyle et al. 2000; Fan et al. 2001). Both PLE and LDDE adequately describe the data, but the LDDE model fits the data slightly better, with significantly higher likelihood. Inspecting the number density of FSRQs of different luminosities confirms they peak at different redshifts, with more luminous FSRQs peaking earlier in time.

Although both PLE and LDDE evolutionary models give good fits to the data, the two models diverge substantially beyond the radio-flux limit. In particular, the LDDE model predicts tens of millions more sources at high redshift ($z \gtrsim 4$), with low luminosities that are well below the detection threshold, while the PLE model predicts fewer FSRQs above the redshift peak of $z \sim 2$. This is mainly due to the lack of a cutoff in the evolution of low-luminosity objects, which can be seen in Figure 9. To distinguish between extrapolations of these models (i.e., to measure the evolution of lower luminosity FSRQs) requires deeper observations.

This radio LF, being the most accurate one using the most complete FSRQ sample, enables further studies, such as simulating cosmic backgrounds, constraining relativistic beaming, or carrying out population studies.

This publication makes use of data products from the Wide-field Infrared Survey Explorer, which is a joint project of the University of California, Los Angeles, and the Jet Propulsion Laboratory/California Institute of Technology, funded by the National Aeronautics and Space Administration.

Funding for SDSS-III has been provided by the Alfred P. Sloan Foundation, the participating institutions, the National Science Foundation, and the US Department of Energy Office of Science. The SDSS-III website is http://www.sdss3.org/. SDSS-III is managed by the Astrophysical Research Consortium for the Participating Institutions of the SDSS-III Collaboration, including the University of Arizona, the Brazilian Participation Group, Brookhaven National Laboratory, Carnegie Mellon University, University of Florida, the French Participation Group, the German Participation Group, Harvard University, the Instituto de Astrofisica de Canarias, the Michigan State/Notre Dame/JINA Participation Group, Johns Hopkins University, Lawrence Berkeley National Laboratory, Max Planck Institute for Astrophysics, Max Planck Institute for Extraterrestrial Physics, New Mexico State University, New York University, Ohio State University, Pennsylvania State University, University of Portsmouth, Princeton University, the Spanish Participation Group, University of Tokyo, University of Utah, Vanderbilt University, University of Virginia, University of Washington, and Yale University.

Part of this work is based on archival data, software, or online services provided by the ASI Science Data Center.

The NASA/IPAC Extragalactic Database (NED) is operated by the Jet Propulsion Laboratory, California Institute of Technology, under contract with the National Aeronautics and Space Administration.

TOPCAT[14] (Taylor 2005) was used for the preparation and manipulation of the tabular data and the images.

F. M. gratefully acknowledges the financial support of the Programma Giovani Ricercatori—Rita Levi Montalcini—Rientro dei Cervelli (2012) awarded by the Italian Ministry of Education, Universities and Research (MIUR).

References

Ahn, C. P., Alexandroff, R., Allende Prieto, C., et al. 2012, ApJS, 203, 21
Ajello, M., Costamante, L., Sambruna, R. M., et al. 2009, ApJ, 699, 603
Ajello, M., Shaw, M. S., Romani, R. W., et al. 2012, ApJ, 751, 108

[14] http://www.star.bris.ac.uk/~mbt/topcat/

Alam, S., Albareti, F. D., Allende Prieto, C., et al. 2015, ApJS, 219, 12
Assef, R. J., Stern, D., Kochanek, C. S., et al. 2013, ApJ, 772, 26
Avni, Y. 1976, ApJ, 210, 642
Beckmann, V., Engels, D., Bade, N., & Wucknitz, O. 2003, A&A, 401, 927
Blandford, R. D., & Rees, M. J. 1978, Phys. Scr., 17, 265
Blandford, R. D., & Znajek, R. L. 1977, MNRAS, 179, 433
Boyle, B. J., Shanks, T., Croom, S. M., et al. 2000, MNRAS, 317, 1014
Breiman, L. 2001, Mach. Learn., 45, 5
Caccianiga, A., Maccacaro, T., Wolter, A., Della Ceca, R., & Gioia, I. M. 2002, ApJ, 566, 181
Chiang, J., & Mukherjee, R. 1998, ApJ, 496, 752
Cortes, C., & Vapnik, V. 1995, Mach. Learn., 20, 273
D'Abrusco, R., Massaro, F., Ajello, M., et al. 2012, ApJ, 748, 68
D'Abrusco, R., Massaro, F., Paggi, A., et al. 2013, ApJS, 206, 12
D'Abrusco, R., Massaro, F., Paggi, A., et al. 2014, ApJS, 215, 14
Falomo, R., Pian, E., & Treves, A. 2014, A&ARv, 22, 73
Fan, X., Strauss, M. A., Schneider, D. P., et al. 2001, AJ, 121, 54
Fossati, G., Celotti, A., Ghisellini, G., & Maraschi, L. 1997, MNRAS, 289, 136
Friedman, J. H. 2001, AnSta, 29, 1189
Giommi, P., Ansari, S. G., & Micol, A. 1995, A&AS, 109, 267
Giommi, P., Colafrancesco, S., Padovani, P., et al. 2009, A&A, 508, 107
Giommi, P., & Padovani, P. 1994, MNRAS, 268, L51
Giroletti, M., Massaro, F., D'Abrusco, R., et al. 2016, A&A, 588, A141
Gregory, P. C., Scott, W. K., Douglas, K., & Condon, J. J. 1996, ApJS, 103, 427
Hartman, R. C., Bertsch, D. L., Bloom, S. D., et al. 1999, ApJS, 123, 79
Hasinger, G., Miyaji, T., & Schmidt, M. 2005, A&A, 441, 417
Healey, S. E., Romani, R. W., Taylor, G. B., et al. 2007, ApJS, 171, 61
Helfand, D. J., White, R. L., & Becker, R. H. 2015, ApJ, 801, 26
Hinshaw, G., Larson, D., Komatsu, E., et al. 2013, ApJS, 208, 19
Jarrett, T. H., Cohen, M., Masci, F., et al. 2011, ApJ, 735, 112
Kimball, A. E., & Ivezić, Ž. 2008, AJ, 136, 684
Kuehr, H., Witzel, A., Pauliny-Toth, I. I. K., & Nauber, U. 1981, A&AS, 45, 367
Mao, P., Urry, C. M., Massaro, F., et al. 2016, ApJS, 224, 26
Marshall, H. L., Tananbaum, H., Avni, Y., & Zamorani, G. 1983, ApJ, 269, 35
Massaro, E., Maselli, A., Leto, C., et al. 2015, Ap&SS, 357, 75
Massaro, F., & D'Abrusco, R. 2016, ApJ, 827, 67
Massaro, F., D'Abrusco, R., Ajello, M., Grindlay, J. E., & Smith, H. A. 2011, ApJL, 740, L48
Massaro, F., D'Abrusco, R., Giroletti, M., et al. 2013a, ApJS, 207, 4
Massaro, F., D'Abrusco, R., Paggi, A., et al. 2013b, ApJS, 209, 10
Massaro, F., D'Abrusco, R., Paggi, A., et al. 2013c, ApJS, 206, 13
Massaro, F., Giroletti, M., D'Abrusco, R., et al. 2014a, ApJS, 213, 3
Massaro, F., Giroletti, M., Paggi, A., et al. 2013d, ApJS, 208, 15
Massaro, F., Masetti, N., D'Abrusco, R., Paggi, A., & Funk, S. 2014b, AJ, 148, 66
Mateos, S., Alonso-Herrero, A., Carrera, F. J., et al. 2013, MNRAS, 434, 941
Nori, M., Giroletti, M., Massaro, F., et al. 2014, ApJS, 212, 3
Padovani, P., Giommi, P., Landt, H., & Perlman, E. S. 2007, ApJ, 662, 182
Padovani, P., & Urry, C. M. 1990, ApJ, 356, 75
Padovani, P., & Urry, C. M. 1991, ApJ, 368, 373
Padovani, P., & Urry, C. M. 1992, ApJ, 387, 449
Peterson, B. M. 1997, Obs, 117, 314
Pracy, M. B., Ching, J. H. Y., Sadler, E. M., et al. 2016, MNRAS, 460, 2
Rector, T. A., Stocke, J. T., Perlman, E. S., Morris, S. L., & Gioia, I. M. 2000, AJ, 120, 1626
Ricci, R., Prandoni, I., Gruppioni, C., Sault, R. J., & de Zotti, G. 2006, A&A, 445, 465
Salamon, M. H., & Stecker, F. W. 1994, ApJL, 430, L21
Schmidt, M. 1968, ApJ, 151, 393
Schmidt, M., Schneider, D. P., & Gunn, J. E. 1995, AJ, 110, 68
Stern, D., Assef, R. J., Benford, D. J., et al. 2012, ApJ, 753, 30
Stern, D., Eisenhardt, P., Gorjian, V., et al. 2005, ApJ, 631, 163
Stickel, M., Padovani, P., Urry, C. M., Fried, J. W., & Kuehr, H. 1991, ApJ, 374, 431
Taylor, M. B. 2005, in ASP Conf. Ser. 347, Astronomical Data Analysis Software and Systems XIV, ed. P. Shopbell, M. Britton, & R. Ebert (San Francisco, CA: ASP), 29
Ueda, Y., Akiyama, M., Ohta, K., & Miyaji, T. 2003, ApJ, 598, 886
Urry, C. M., & Padovani, P. 1995, PASP, 107, 803
Véron-Cetty, M. P., & Véron, P. 2000, A&ARv, 10, 81
Wall, J. 2008, arXiv:0807.3792
Wall, J. V., Jackson, C. A., Shaver, P. A., Hook, I. M., & Kellermann, K. I. 2005, A&A, 434, 133
White, R. L., Becker, R. H., Helfand, D. J., & Gregg, M. D. 1997, ApJ, 475, 479
Wolter, A., & Celotti, A. 2001, A&A, 371, 527